Methodology and Numerical Strategy for Forecasting the Leakage Rate Evolution of Nuclear Reactor Buildings Inner Containments

Mehdi ASALI[1,2,*], Bruno CAPRA[1], Jacky MAZARS[1] and Jean-Baptiste COLLIAT[2]

[*]Corresponding author: mehdi.asali@oxand.com

[1]OXAND France, 49 avenue F. Roosevelt, 77210 Avon, France

[2]Univ. Lille, CNRS, Centrale Lille, Arts et Métiers Paris Tech, FRE 3723 – LML – Laboratoire de Mécanique de Lille, Boulevard Paul Langevin, Cité Scientifique, 59655 Villeneuve d'Ascq Cedex, France

Abstract

The containment building represents the third and last protection barrier of nuclear reactors buildings (NRB). Yet ageing mechanisms of prestressed concrete could strongly affect the tightness capacity of the inner containment of a double-wall reactor building over time. That is a major issue considering the long-term operation and the potential life extension of NRBs while ensuring safety and regulatory requirements. Considering the size of those structures and the complexity of all interacting phenomena (such as drying, creep, shrinkage and cracking), it is very difficult from a computational perspective to build an industrial and operational tool modeling efficiently all the strong couplings occurring at different scales. In that context, a simple yet physically representative chained weakly-coupled strategy based on a macro-element discretization is implemented and applied to the VeRCoRs mock-up (scale 1:3). The proposed methodology adapts to feedback and data collected with time. It enables operators (1) to take into account variabilities and uncertainties of main parameters in order to quantify their impact on the total leakage rate, (2) to manually introduce defects coming from visual inspections and (3) to preempt and optimize leak mitigation actions in order to avoid outage extensions and associated losses of income.

Keywords: Porous and cracked concrete / Air leakage / Inner containment wall / Ageing / Long-term operation

Nomenclature

Symbol	Unit	Description
A	-	μ-model parameter
B	-	μ-model parameter
C_p	$J \cdot kg^{-1} \cdot K^{-1}$	Concrete's thermal capacity
d	-	Scalar effective damage field (values between 0 and 1)
D	$m^2 \cdot s^{-1}$	Liquid water diffusion coefficient
E	Pa	Young's modulus of concrete
E_a	$J \cdot mol^{-1}$	Thermal activation energy of concrete
$\mathbf{I_3}$	-	3D identity matrix
I_S	-	Sensitivity index
K_{int}^{g}	m^2	Gaseous air intrinsic permeability of concrete
K_{int}^{l}	m^2	Liquid water intrinsic permeability of concrete
k_{irr}	Pa	Stiffness associated to the non-reversible ageing dashpot for basic creep
k_{rev}	Pa	Stiffness associated to the reversible basic creep strains
k_{rg}	-	Gaseous air relative permeability of concrete (values between 0 and 1)
k_{rl}	-	Liquid water relative permeability of concrete (values between 0 and 1)
m	-	Parameter of Van Genuchten's model
M_g	$kg \cdot mol^{-1}$	Air molar mass
n	-	Parameter of Van Genuchten's model
$\mathbf{n_e}$		Normed normal vector to the crack in a finite element
P_c	Pa	Capillary pressure
P_g	Pa	Gaseous air pressure field
P^{norm}	Pa	Normal pressure (1 atm, 101315 Pa)
P_r	Pa	Parameter of Van Genuchten's model
$\mathbf{q_D}$	$kg \cdot s^{-1} \cdot m^{-2}$	Air flux field within concrete matrix (Darcy's law)
$\mathbf{q_P}$	$kg \cdot s^{-1} \cdot m^{-2}$	Air flux field the crack (Poiseuille's law)
Q_M	$kg \cdot s^{-1}$	Total mass air leak rate

Q_V^{norm}	$Nm^3 \cdot h^{-1}$	Normalized total volumetric air leakage rate
R	$J \cdot mol^{-1} \cdot K^{-1}$	Universal gas constant
S_l	-	Liquid water saturation of concrete (values between 0 and 1)
Sp( )		Spectrum of a square matrix (set of its eigenvalues)
t	s	Time
t_{ini}	s	Starting time of computations
T	K	Temperature
T^{norm}	K	Normal temperature (0 °C , 273.15 K)
T^{ref}	K	Reference temperature for material properties
tr( )		Trace operator on a square matrix
w_e	m	Crack opening of a finite element
$\boldsymbol{x}$		Spatial position (vector of coordinates)
Y	-	μ-model driving variable
Y_0	-	Initial threshold of variable Y
α_s	K^{-1}	Thermal expansion coefficient of steel
α_{th}	K^{-1}	Thermal expansion coefficient of concrete
$\boldsymbol{\varepsilon}$	-	Total strain tensor in concrete
$\boldsymbol{\varepsilon}^{\mathbf{bc}}$	-	Basic creep strain tensor in concrete
$\boldsymbol{\varepsilon}_{\mathbf{cod}}$	-	Crack-effective strain tensor
ε_{cor}	-	Corrected measured strain
$\boldsymbol{\varepsilon}^{\mathbf{dc}}$	-	Drying creep strain tensor in concrete
$\boldsymbol{\varepsilon}^{\mathbf{ds}}$	-	Drying shrinkage strain tensor in concrete
$\boldsymbol{\varepsilon}^{\mathbf{el}}$	-	Damaged elastic strain tensor in concrete
$\boldsymbol{\varepsilon}^{\mathbf{irr}}$	-	Irreversible part of basic creep strain tensor
ε_{raw}		Raw measured strain
$\boldsymbol{\varepsilon}^{\mathbf{rev}}$	-	Reversible part of basic creep strain tensor
$\boldsymbol{\varepsilon}^{\mathbf{th}}$	-	Thermal expansion strain tensor in concrete
ζ	-	Coefficient for Poiseuille's flow reduction within cracks (values between 0 and 1).
η_g	Pa·s	Gaseous air viscosity
η_l	Pa·s	Liquid water viscosity

η_{rev}	Pa·s	Viscosity associated to the reversible creep strains
κ_{dc}	Pa^{-1}	Drying creep coefficient of concrete
κ_{ds}	-	Drying shrinkage coefficient of concrete
λ	$W \cdot m^{-1} \cdot K^{-1}$	Concrete's thermal conductivity
ν	-	Elastic Poisson's ratio of concrete
ν_{bc}	-	Basic creep Poisson's ratio
ρ_b	$kg \cdot m^{-3}$	Concrete's density
$\boldsymbol{\sigma}$	Pa	Stress tensor in concrete
$\tilde{\boldsymbol{\sigma}}$	Pa	Effective stress tensor in concrete
Σ_e	m^2	Crack area in a finite element
ϕ	-	Concrete's porosity (value between 0 and 1)
Ω_e	m^3	Size of a finite element
$\boldsymbol{\nabla}$	m^{-1}	Differential "nabla" operator

1 Introduction

Nuclear reactor buildings (NRB) of pressurized water reactors have three main safety functions: reactor power control, nuclear fuel cooling and radioactive products containment. The latter safety function is ensured by three safety barriers built on the Russian dolls principle: the nuclear fuel sheath, the primary coolant system casing and the containment building. EDF, the French nuclear operator, manage two different containment building technologies: 34 single-wall assets with a steel liner (900 MWe) and 24 double-wall assets without liner (1300 and 1450 MWe). Those containment buildings being irreplaceable, their airtightness is periodically controlled during decennial internal leakage rate tests (ILRT) for obtaining, if safety is ensured, an extra 10-year operating authorization from the regulator.

In the case of double-wall containment, the leak tightness is mostly ensured by an inner containment wall built in prestressed and reinforced concrete, together with a continuous filtering of the air volume between the inner and outer containment walls. Ageing mechanisms of the concrete structure, linked to the coupling of desiccation, creep, shrinkage, prestressing losses or cracking, lead to a decrease of its airtightness capacity over time. If not anticipated before a decennial test, the restart of the unit could be jeopardized leading to potentially important losses of income (unit outage extension, setup of expansive mitigation or repair techniques). Moreover, the fleet is approaching its initially designed 40-year lifetime and EDF consider extending operation up to 60 years.

In that context of long-term operation and life extension of NRB while maintaining safety, EDF has built an inner containment experimental mock-up at scale 1/3 called VeRCoRs ("VErification Réaliste du COnfinement des RéacteurS" [1]). The chosen scale accelerates drying (diffusive phenomena) by a factor of 9 compared to full-size structures so as to provide EDF with data representative of a 60-year old NRB around 2021. Main goals of the VeRCoRs project are to [2]:

- Experimentally demonstrate the robustness of inner containments in accidental situations up to 60 years,
- Improve knowledge on thermo-hydro-mechanical (THM) mechanisms at the origin of air leakage rate increase,
- Test new methods for detecting and measuring leaks,
- Test new techniques to repair or improve airtightness,
- Improve modeling tools to forecast the leakage rate evolution.

This last point will be made possible by benchmarking simulations to numerous experimental data coming from heavy monitoring of the mock-up (vibrating wires, temperature sensors, optical fibers, weather station, etc.) and large material characterization from over 1000 samples.

In order to model the complex THM behavior of inner containments and to tackle the general problematic of leakage rate evolution, multiscale and multiphysics expertise becomes necessary. In the more particular case of global strategies practical for industrial purposes, a good compromise should be reached between the refinement of discretization, the nonlinearity of behavior laws and strong

couplings, justifying their sparsity in the literature. A first family of strategies concentrates on a better representativeness of physical phenomena by using strongly nonlinear and coupled laws [3-7]. They need refined discretization to enable numerical convergence, often limiting their scope to structurally representative volumes of few cubic meters. A second family concentrates on computations at the structural scale by simplifying the geometry thus reducing numerical costs [8-10] (2D axisymmetric sections, rebars or tendons homogenization within concrete thickness with multilayer shell elements, etc.). Those strategies enable to assess an average behavior of the structure but cannot represent singularities and heterogeneities such as hatches, tendons deviations or variable humidity within concrete thickness. A last family concentrates on keeping the geometrical complexity of inner containments through detailed meshing but only considers elastic or viscoelastic structural behavior [11-14]. The reduced cost of those methods is appealing from an engineering point of view. Nevertheless, they lack some post-peak behavior for concrete and consequently lead to non-representative stress fields in singular areas that are used afterwards to post-treat cracks spacing and openings with design codes formulae [15].

In this respect, a methodology and a tool for computing and forecasting the air leakage rate of inner containments have been developed for industrial and operational purposes. After describing the modeling principles underlying the proposed numerical THM strategy and validating those choices on the VeRCoRs mock-up, this study focuses on practical industrial applications and on the

contribution of the proposed tool to the ageing management of NRB inner containments.

2 Numerical Strategy for Computing the Leakage Rate of an Inner Containment

2.1 Modeling Principles

Considering the size of the studied structures and the complexity of all interacting phenomena, it is very difficult from a computational perspective to build an industrial and operational tool finely and fully modeling all the strong couplings. To simplify the problem, a chained weakly-coupled methodology (Fig. 1) has been implemented. It is based on a 3D macro finite element discretization and aims at representing at lower numerical cost the physical behavior of an inner containment under operating conditions. Thus, early age behavior of concrete during erection and accidental situations with high and quick variations of pressure and temperature are out of the scope of this study.

Main goals of this simplified - but not simplistic - approach are to:

- Compute air leakage through porous and cracked concrete in a practical way,
- Be able to take into account variability and uncertainty of the main material parameters while keeping acceptable computation times for industrial use,
- Increase the value of field data, either monitored occasionally (e.g. total leakage rate) or continuously (e.g. delayed strains), by using this data as input to adapt or calibrate the tool and improve forecasts over time.

Complete details on the numerical methodology can be found in [16-17] and only the main assumptions and ingredients are summarized in this section.

2.1.1 Thermal Model

In a first step, the temperature field $T(\boldsymbol{x}, t)$ (in K) is computed independently of all other phenomena. Heat transfer is mainly caused by thermal conduction within concrete's volume and follows the classical heat equation (1):

$$\rho_b C_p \frac{\partial T(\boldsymbol{x}, t)}{\partial t} + \boldsymbol{\nabla} \cdot [-\lambda(T) \boldsymbol{\nabla} T(\boldsymbol{x}, t)] = 0 \qquad (1)$$

Where ρ_b is the concrete density (in kg·m^{-3}), C_p is the concrete thermal capacity (J·kg^{-1}·K^{-1}) and λ is the concrete thermal conductivity field (in W·m^{-1}·K^{-1}). In a classical way, boundary conditions of the thermal problem can be expressed with imposed temperatures, convective exchanges or thermal radiations.

2.1.2 Hydric Model

In a second step, the water saturation field $S_l(\boldsymbol{x}, t)$ in concrete is computed. Humidity staying above 40% in concrete during inner containments operation, the following assumptions are typically considered [18-22]:

- Drying is mainly due to liquid water movements within concrete porosity,
- Drying/soaking cycles during the pre-operational phase only impact boundary concrete, not core concrete,
- Air pressure is negligible compared to water pressure.

In that case, a classical non-linear diffusion equation (2) is used, where the diffusion coefficient $D(S_l, T)$ depends on temperature as proposed by [18]:

$$\frac{\partial S_l(\boldsymbol{x},t)}{\partial t} + \boldsymbol{\nabla}\cdot[D(S_l,T)\boldsymbol{\nabla}S_l(\boldsymbol{x},t)] = 0 \quad (2a)$$

$$D(S_l,T) = \frac{K_{int}^l k_{rl}(S_l)}{\eta_l \phi}\frac{\partial P_c}{\partial S_l}\frac{T(\boldsymbol{x},t)}{T^{ref}}\exp\left(\frac{E_a}{R}\left(\frac{1}{T^{ref}} - \frac{1}{T}\right)\right) \quad (2b)$$

Where K_{int}^l is the water intrinsic permeability of concrete (in m^2), k_{rl} is the water relative permeability field (values between 0 and 1), η_l is the water viscosity (in Pa·s), ϕ is the concrete porosity, P_c is the capillary pressure field (in Pa), T^{ref} is the reference temperature (in K) at which all hydric properties of equation (2) are defined or measured, E_a is the thermal activation energy of concrete (in $J{\cdot}mol^{-1}$), R is the universal gas constant (in $J{\cdot}mol^{-1}{\cdot}K^{-1}$).

The capillary pressure is defined with Van Genuchten's retention model [23]:

$$P_c(S_l) = P_r\left(S_l^{-1/m} - 1\right)^{1/n} \quad (3)$$

Where P_r (in Pa) and n (> 1) are model parameters and $m = 1 - 1/n$. The water relative permeability follows Mualem's model [24]:

$$k_{rl}(S_l) = \sqrt{S_l}\left[1 - \left(1 - S_l^{1/m}\right)^m\right]^2 \quad (4)$$

2.1.3 Mechanical Model

In a third step, delayed strains in concrete are computed. Prestressing losses in tendons are modeled according to ETC-C formulae [25] considering a perfect bond between concrete and steel cables. Passive reinforcement bars are not explicitly taken into account. The total strain field $\boldsymbol{\varepsilon}(\boldsymbol{x},t)$ is split into five main components representative of operating conditions:

$$\boldsymbol{\varepsilon}(\boldsymbol{x},t) = \boldsymbol{\varepsilon}^{\mathbf{el}} + \boldsymbol{\varepsilon}^{\mathbf{bc}} + \boldsymbol{\varepsilon}^{\mathbf{dc}} + \boldsymbol{\varepsilon}^{\mathbf{ds}} + \boldsymbol{\varepsilon}^{\mathbf{th}} \quad (5)$$

Where $\boldsymbol{\varepsilon}^{\mathbf{el}}$ is the damaged elastic strain tensor, $\boldsymbol{\varepsilon}^{\mathbf{bc}}$ is the basic creep tensor, $\boldsymbol{\varepsilon}^{\mathbf{dc}}$ is the drying creep tensor, $\boldsymbol{\varepsilon}^{\mathbf{ds}}$ is the drying shrinkage tensor and $\boldsymbol{\varepsilon}^{\mathbf{th}}$ is the thermal expansion tensor.

Thermal expansion and drying shrinkage are considered as isotropic and proportional to temperature and saturation respectively [26, 18]:

$$\boldsymbol{\varepsilon}^{\mathbf{th}}(\boldsymbol{x},t) = \alpha_{th}\big(T(\boldsymbol{x},t) - T(\boldsymbol{x},0)\big)\mathbf{I_3} \tag{6}$$

$$\boldsymbol{\varepsilon}^{\mathbf{ds}}(\boldsymbol{x},t) = \kappa_{ds}\big(S_l(\boldsymbol{x},0) - S_l(\boldsymbol{x},t)\big)\mathbf{I_3} \tag{7}$$

Where α_{th} is the thermal expansion coefficient (in K^{-1}), κ_{ds} is the drying shrinkage coefficient (no unit) and $\mathbf{I_3}$ is the 3D identity matrix.

Drying creep is considered as proportional to the effective stress $\tilde{\boldsymbol{\sigma}}$ (in Pa) and saturation states of concrete as suggested by [27, 28] to model Pickett's effect [29]:

$$\dot{\boldsymbol{\varepsilon}}^{\mathbf{dc}}(\boldsymbol{x},t) = \kappa_{dc}\big|\dot{S}_l(\boldsymbol{x},t)\big|\tilde{\boldsymbol{\sigma}}(\boldsymbol{x},t) \tag{8}$$

Where κ_{dc} is the drying creep coefficient (in Pa^{-1}).

Basic creep is modeled with an ageing Burger's rheological chain (9), as suggested by [27]. This choice enables to take into account biaxial creep effects (10, 11), a logarithmic evolution of creep strains over time (12) and the impact of pre-computed temperature and saturation fields on creep parameters (12, 13).

$$\boldsymbol{\varepsilon}^{\mathbf{bc}}(\boldsymbol{x},t) = \boldsymbol{\varepsilon}^{\mathbf{rev}}(\boldsymbol{x},t) + \boldsymbol{\varepsilon}^{\mathbf{irr}}(\boldsymbol{x},t) \tag{9}$$

$$\hat{\eta}_{am}(t)\dot{\boldsymbol{\varepsilon}}^{\mathbf{irr}} = (1+\nu_{bc})\boldsymbol{\sigma} - \nu_{bc}\mathrm{tr}(\boldsymbol{\sigma})\mathbf{I_3} \tag{10}$$

$$\hat{\eta}_{kv}\dot{\boldsymbol{\varepsilon}}^{\mathbf{rev}} + \hat{k}_{kv}\boldsymbol{\varepsilon}^{\mathbf{rev}} = (1+\nu_{bc})\tilde{\boldsymbol{\sigma}} - \nu_{bc}\mathrm{tr}(\tilde{\boldsymbol{\sigma}})\mathbf{I_3} \tag{11}$$

$$\hat{\eta}_{irr}(t,T,S_l) = \frac{k_{irr}t}{S_l}\exp\left(\frac{E_a}{R}\left(\frac{1}{T} - \frac{1}{T_{ref}}\right)\right) \tag{12}$$

$$\hat{\Xi}_{rev}(T, S_l) = \frac{\Xi_{rev}}{S_l} \exp\left(\frac{E_a}{R}\left(\frac{1}{T} - \frac{1}{T_{ref}}\right)\right), \qquad \Xi \in \{k, \eta\} \tag{13}$$

Where $\boldsymbol{\varepsilon}^{\mathbf{rev}}$ is the reversible basic creep strain field, $\boldsymbol{\varepsilon}^{\mathbf{irr}}$ is the non-reversible creep strain field, $\boldsymbol{\sigma}$ is the total stress tensor field in concrete, ν_{bc} is the basic creep Poisson's ratio, k_{irr} is the stiffness associated to the non-reversible ageing dashpot (in Pa), k_{rev} is the stiffness associated to the reversible creep strains (in Pa), η_{rev} is the viscosity associated to the reversible creep strains (in Pa·s).

Concrete's post-peak behavior is modeled with the μ-model [30] in order to take into account a unilateral effect (crack closing and reopening) that could occur with cycling ILRT.

$$E\boldsymbol{\varepsilon}^{\mathbf{el}}(\boldsymbol{x}, t) = (1 + \nu)\tilde{\boldsymbol{\sigma}} - \nu \operatorname{tr}(\tilde{\boldsymbol{\sigma}})\mathbf{I_3} \tag{14}$$

$$\boldsymbol{\sigma}(\boldsymbol{x}, t) = (1 - d)\tilde{\boldsymbol{\sigma}}(\boldsymbol{x}, t) \tag{15}$$

$$d(\boldsymbol{x}, t) = 1 - \frac{(1 - A)Y_0}{Y(\boldsymbol{\varepsilon}^{\mathbf{el}})} - A\exp\left(B\left(Y_0 - Y\left(\boldsymbol{\varepsilon}^{\mathbf{el}}\right)\right)\right) \tag{16}$$

Where E is the Young's modulus of concrete (in Pa), ν its Poisson's ratio, d is the scalar effective damage variable field (values between 0 and 1, a non-null value meaning active cracking either in tension or compression), A and B are coefficients depending on the stress state of concrete and defined from post-peak responses of concrete in pure tension and pure compression, Y is a driving variable for damage evolution and Y_0 is the initial threshold of variable Y. To limit mesh sensitivity due to the softening behavior of concrete, parameter B is adjusted together with element sizes [31].

2.1.4 Air Leakage Model

In a final step, total air leakage is computed. Although cracks in concrete are small and localized for large structures as inner containments, they could represent a preferential pathway for air leakage. Thus, a dedicated 3D finite element has been developed that introduces an equivalent cracking state without explicitly meshing those defects. Its principle (Fig. 2) is to superimpose a Darcy's flow (18) within the unsaturated porous concrete matrix of size Ω_e (in m^3) and a Poiseuille's flow (19) within a perfectly plane crack of area Σ_e (in m^2), opening w_e (in m) and normed normal vector $\mathbf{n_e}$. Considering a stationary and compressible laminar flow and air as a perfect gas, mass conservation leads to solve the non-linear diffusion equation (17):

$$\boldsymbol{\nabla} \cdot \mathbf{q_D} + \boldsymbol{\nabla} \cdot \mathbf{q_P} = 0 \tag{17}$$

$$\mathbf{q_D}(\boldsymbol{x}, t) = -\frac{M_g}{RT(\boldsymbol{x}, t)} \frac{K_{int}^g k_{rg}(S_l)}{2\eta_g} \boldsymbol{\nabla} P_g^2(\boldsymbol{x}, t) \tag{18a}$$

$$k_{rg}(S_l) = \sqrt{1 - S_l}\left(1 - S_l^m\right)^{m/2} \tag{18b}$$

$$\mathbf{q_P}(\boldsymbol{x}, t) = -\frac{M_g}{RT(\boldsymbol{x}, t)} \frac{\zeta \Sigma_e w_e^3}{24 \Omega_e \eta_g} (\mathbf{I_3} - \mathbf{n_e} \otimes \mathbf{n_e}) \boldsymbol{\nabla} P_g^2(\boldsymbol{x}, t) \tag{19}$$

Where $\mathbf{q_D}$ and $\mathbf{q_P}$ are air flux fields within the matrix and the crack respectively (in $kg \cdot s^{-1} \cdot m^{-2}$), K_{int}^g is the air intrinsic permeability of concrete (in m^2), k_{rg} its air relative permeability field (defined by Mualem's law as modified by [19]), η_g is the air viscosity (in Pa·s), M_g is the air molar mass (in $kg \cdot mol^{-1}$), P_g is the air pressure field (in Pa) and ζ a flow reduction factor to represent tortuosity, roughness or turbulence effects (values between 0 and 1).

Crack openings and orientations in each finite element are obtained according to [7, 32]. A crack-effective strain tensor field $\boldsymbol{\varepsilon_{cod}}$ is defined from the damaged

elastic behavior of concrete (20). Its maximal eigenvalue in tension (if any) is used to compute the crack opening (21) and the associated eigenvector defines the crack surface normal.

$$\boldsymbol{\varepsilon}_{\mathbf{cod}}(\boldsymbol{x},t) = \boldsymbol{\varepsilon}^{\mathbf{el}} - \frac{1}{E}[(1+\nu)\boldsymbol{\sigma} - \nu\,\mathrm{tr}(\boldsymbol{\sigma})\mathbf{I_3}] \tag{20}$$

$$w_e = \sqrt[3]{\Omega_e}\,\max\left[\max\left(\mathrm{Sp}(\boldsymbol{\varepsilon}_{\mathbf{cod}})\right), 0\right] \tag{21}$$

Total leakage corresponding to the quantity of air leaving the internal volume of the inner containment, the total mass leak rate Q_M (in kg·s^{-1}) is computed by projecting nodal air fluxes and integrating over the whole internal surface. In order to compare leakage rates of all NRB independently of each ILRT temperature and pressure conditions, EDF converts mass flow rates into volumetric flow rates expressed at normal temperature and pressure conditions:

$$Q_V^{norm} = 3600\frac{R}{M_g}\frac{T^{norm}}{P^{norm}}Q_M \tag{22}$$

Where Q_V^{norm} is the volumetric total leakage rate (in Nm^3·h^{-1}) at normal temperature T^{norm} (0 °C) and normal pressure P^{norm} (101315 Pa).

2.1.5 Software and Hardware Used

This numerical strategy is implemented within the general framework of Code_Aster v12.3 [33]. Due to the equivalence between equations (1, 2, 17), the same non-linear thermal solver is used for thermal, drying and air-leakage computations and the 3D macro-element dedicated to leakage is developed as new thermal finite element within Code_Aster. The concrete delayed strain model (5-16) is implemented as an external user behavior law with TFEL/MFront v2.0.1 [34] and ETC-C prestressing losses are directly available with Code_Aster [35].

All results of this article were computed on a dedicated server using 24 GB of RAM and 1 Intel® Xeon® processor with 4 cores at 2.67 GHz.

2.2 Validation of the Strategy on the VeRCoRs Mock-up

2.2.1 Mesh

In order to demonstrate the applicability of the proposed macro-element methodology, the coarser mesh given during the first VeRCoRs international benchmark [36] has been used. It includes 34694 nodes in 3D concrete elements (penta- and hexahedra) and 16066 nodes in 1D cable elements (bars). 295 prestressing cables (horizontal, vertical, gamma and dome) and their deviations are taken into account (Fig. 3a). Despite vertical and circumferential coarse meshing of concrete (Fig 3b), the 10-element progressive fineness within the 40 cm thickness is considered suitable to represent thermal and humidity gradients (Fig. 3c).

2.2.2 Boundary Conditions and Loadings

As the overall structure is subject to a changing environment as well as to a complex construction phasing process, the on-site evolutions of loadings and boundary conditions have been simplified before being applied over the whole considered time frame. The main construction planning of the mock-up is assumed as such (Fig. 4):

- Erection is done at once, the starting date of all computations is on 30 November 2014.
- Due to water aspersion on the mock-up's walls, the structure begins to dry only from 1 April 2015.

- Prestressing occurs between 6 May and 12 August 2015 with a reduced number of tensioning steps.
- Two main life phases of the structure are occurring: pre-operational until 28 January 2016 during which the mock-up is subject to its external environment, then operational starting on 1 April 2016. The transition between both phases is linearized.
- The first three ILRT of the mock-up are considered in the present study: two pre-operational tests (PT_0 and PT_1) occurring during 10-14 November 2015 and 24-28 January 2016 respectively, and the first decennial test (DT_1) during 20-24 April 2017.

Soil temperature applied at the bottom of the raft is kept constant during the whole computation at 10.5 °C (initial value). During pre-operation, measurements within concrete are available to calibrate imposed air temperatures. No daily variations are considered, only linear evolutions between extremal values. Operating temperature conditions are 35 °C at the inner side and 15 °C at the outer side of the inner containment. Temperature is kept constant during each decennial test at 10 °C (Fig. 5).

As for temperature, soil humidity is kept constant at 0.98 (initial value). During pre-operation, measurements of the weather station are imposed at the inner and outer sides with linearization between extremal values. Operating humidity conditions are supposed to be 0.45 at the inner side and 0.6 at the outer side of the containment, with no interruption during decennial tests (Fig. 6).

As no early age behavior is considered, initial stress and strain states are null. The bottom of the raft is embedded during the whole computation. Reinforcement bars are not explicitly meshed, but participate in the dead weight of the structure (extra 100 $kg \cdot m^{-3}$ for concrete's density). The raft and anchoring ribs remain visco-elastic without damage. Prestressing is done in only 14 grouped steps (instead of the real 41 sequences in 16 phases), with an initial tension of 848 kN for each cable.

All ILRT pressure loadings applied at the inner side of the containment are identical. They last four days, with a 24-hour ramp from standard atmosphere to maximal pressure (5.2 bar abs.), a 24-hour plateau at maximal pressure and 48 h of deflating (Fig. 7). The raft being submerged during ILRT, it is not considered as a possible leakage pathway (null flux).

2.2.3 Modeling Parameters

If available, concrete parameters are preferably mean values of on-site measurements for each lift (density, porosity, Young's modulus, tensile strength, thermal expansion coefficient). If not, other concrete parameters come or are identified from specific laboratory testing (thermal capacity, linear thermal conductivity with temperature, activation energy, fracture energy, water intrinsic permeability, Van Genuchten's parameters, drying shrinkage coefficient, basic and drying creep parameters) (Fig. 8).

Cable parameters come from design and manufacturer values. The complete set of parameters used for the present study is available in Tab. 1.

2.2.4 Main Results

As temperature is following imposed seasonal variations and humidity measurements are not yet available within VeRCoRs mock-up to validate its drying kinectics modeling, the comparison between measured and computed total strains is considered as the best way to validate the proposed numerical THM strategy. In order to do so, total strains within the mock-up are extracted at four observation points H1, H2, H5 and H6 (Fig. 9) considered as representative of the behavior of the structure in standard areas (far from any change in concrete geometry or tendon deviation). They all lie on the same horizontal plane at mid-height of the cylindrical part and are diametrically opposed, at the inner and outer sides of the containment.

Those points are monitored with vibrating wires and temperature sensors to correct measured vertical and tangential strains from steel thermal expansion (23a). Measured strains are also corrected from the initial null state assumption chosen for the computations (23b).

$$\varepsilon^*_{cor}(t) = \varepsilon_{raw}(t) + \alpha_s\big(T(t) - T(0)\big) \quad (23a)$$

$$\varepsilon_{cor}(t) = \varepsilon^*_{cor}(t) - \varepsilon^*_{cor}(t_{ini}) \quad (23b)$$

Where ε_{raw} is the raw measured strain, α_s is the steel thermal expansion coefficient ($11.5 \cdot 10^{-6}$ K^{-1} according to [36]), ε_{cor} is the corrected measured strain and t_{ini} is the starting time for computations.

In Fig. 10, computed total strains (dashed lines) are compared with available corrected strain measurements (plain lines) until the first ILRT (PT_0). The mechanical computation is then extended to the first decennial test DT_1.

According to Fig. 10a, kinetics of delayed effects as well as strain levels are well reproduced in the vertical direction. According to Fig. 10b, kinetics of delayed effects is well reproduced in the tangential direction, but compressive strain levels are globally underestimated by the model, especially at points H5 and H6. This gap may be explained by the fact that only uniaxial creep tests are available to calibrate a biaxial creep model leading to a homogeneous behavior of concrete in the vertical and tangential directions.

To be more precise in the level of short-term strains, the drying shrinkage model may have to be modified. As shown in Fig. 8b, the chosen model is preferentially able to fit the long-term constant level of strains and is less accurate for the first months. Its impact on the total strain in Fig. 8d remains noticeable for the mock-up during the first months after erection. However, keeping in mind that the strategy aims at representing the long-term behavior of full-size NRB, this effect could be accepted in a first approach.

According to Fig. 10, numerical results between the four considered points show less discrepancy compared to experimental data. The gap between H2 and H5 vertical strains is around 25 % for the computation and 45 % for measurements. For tangential strains, the gap between H1 and H6 is around 10 % for the computation and 25 % for measurements. This observation may be due to the homogeneous mechanical properties taken into account in the computation, which are the mean values of the real scattering of on-site concrete properties between the different lifts. Lower scattering of numerical and experimental tangential strains compared with the vertical ones is due to the fact that all four points were

taut together in the horizontal direction (they are at the same height), which was not the case in the vertical direction (they are diametrically opposed).

This overall good forecast of delayed strains coupling THM effects within the mock-up is a first validation of the proposed methodology and numerical strategy.

3 Practical Applications for Decision Support

This section presents three case studies linked to the global air leakage of inner containments to illustrate the potential of the methodology to support operators in their long-term asset management.

3.1 Leakage Forecast of Inner Containments

With the proposed strategy, computation and forecast of water saturation and delayed strains enable assessing the anisotropic apparent permeability linked to the drying of sound concrete and cracks openings (18, 19) and thus the evolution of air leakage of inner containments with time. Nevertheless, not only the global air leakage of the structure should be accurately forecast, but also its distribution by main areas in order to be physically representative of local defects (such as cracks, porosity lines, concrete construction joints, etc.). For instance, on the VeRCoRs mock-up, available air leak measurements and distribution between the hatch, the gusset, the dome and the cylindrical part are given in Tab. 2.

Tab. 2 shows the utmost influence of the gusset in the total leak rate of the mock-up (more than 55 % of total leakage). This experimental observation is due to early age cracks that have been closed by prestressing and afterwards reopen

during IRLT (Fig. 11). However, those cracks remain too small (i.e. opening under 100 μm) to be measurable.

Another parameter which is difficult to assess on-site is the air intrinsic permeability of concrete. Using the mean value of VeRCoRs lifts measurements ($3.13 \cdot 10^{-16}$ m^2, with $1.33 \cdot 10^{-16}$ m^2 standard deviation), that could not be corrected from Klinkenberg's effect [37] due to lack of data, results in overestimating the total leakage rate computed during PT_0 (39.6 Nm^3·h^{-1}, namely five times higher than the experiment).

In order to perform a reverse analysis of those two main inputs, the air leak during PT_0 has been computed with 12 cracks that have been manually patched within the gusset's 3D mesh. To simplify the demonstration, those cracks are perfectly vertical, going through the gusset thickness and evenly distributed along the containment circumference. They all have the same unknown opening w with a prefixed flow reduction factor ζ (according to equation (19), both w and ζ cannot be identified simultaneously). The unknown air intrinsic permeability K_{int}^{g} is homogeneous in the whole concrete structure. Two constraints must be complied with to solve the problem: the total leakage rate of the containment as well as the local leakage of the gusset should be identical to measurements (less than 1 % error). Two different values for ζ are considered in Tab. 3: 1.0 (no flow reduction) and 0.1 (mean value of experimental data found in the literature [38-40, 6]).

Tab. 3 shows that the value identified for K_{int}^{g} in the whole containment ($2.11 \cdot 10^{-17}$ m^2) is independent of the product ζw^3 of equation (19) in the gusset and a

simple law could be used to find the crack opening function of the flow reduction factor:

$$\forall \zeta \in]0\,;1], \qquad w(\zeta) = w(\zeta = 1) \cdot \zeta^{-1/3} \tag{24}$$

The mean value of ζ leads to a 47 µm mean crack opening within the gusset, which is consistent with the on-site measurement difficulty under 100 µm. Fig. 12 illustrates the air flux map of this computation and the local influence of cracks in the gusset. The same methodology could be applied to other areas of interest (hatch, cylinder and dome) or even to every defect identified for which the local leak rate has been measured.

Once unknown parameters have been identified with data of the first ILRT, it is possible to forecast the leakage rate evolution of the mock-up over time (Tab. 4). Indeed, ageing effects of the mock-up are well reproduced by the proposed methodology for PT_1. For the time being, a slightly higher evolution is forecast between PT_1 and DT_1 due to a new crack opening that would need to be experimentally confirmed with future data.

3.2 Sensitivity Analyses

Due to the lack of knowledge on the air intrinsic permeability of concrete and on the air flow reduction factor, this section aims at quantifying the impact of uncertainty of the flow reduction factor (ζ) and of the variability of the intrinsic air permeability (K_{int}^{g}) on the total leakage rate Q of the mock-up. As total leakage is a strictly increasing function of those two parameters (18a, 19), a min-max approach is introduced with the definition of two sensitivity indices I_S:

$$I_S(\zeta) = \frac{Q(\zeta_{max},\ K_{ref}) - Q(\zeta_{min},\ K_{ref})}{Q(\zeta_{ref},\ K_{ref})} \frac{\zeta_{ref}}{\zeta_{max} - \zeta_{min}} \quad (25a)$$

$$I_S(K_{int}^g) = \frac{Q(\zeta_{ref},\ K_{max}) - Q(\zeta_{ref},\ K_{min})}{Q(\zeta_{ref},\ K_{ref})} \frac{K_{ref}}{K_{max} - K_{min}} \quad (25b)$$

Where ζ_{ref}, ζ_{min} et ζ_{max} are respectively reference, minimal and maximal values of ζ and K_{ref}, K_{min} et K_{max} are respectively reference, minimal and maximal values of K_{int}^g. Reference values are those identified in the previous computation ($K_{ref} = 2.11 \cdot 10^{-17}$ m^2 and $\zeta_{ref} = 0.1$).

The interval of variation of ζ is identified in the literature [38-40, 6] ($\zeta_{min} = 0.01$ and $\zeta_{max} = 0.3$). With computation results of Tab. 5, $I_S(\zeta) = 0.64$.

The interval of variation of K_{int}^g is arising from experimental lift measurements whose relative standard deviation (RST) is 42.4 %. To keep 90 % of measured values, the RST is multiplied by 1.64 (meaning ±69.7 %). With computation results of Tab. 6, $I_S(K_{int}^g) = 0.36$.

In conclusion, for the PT_0 case modeled where 12 cracks of 47 µm opening are evenly distributed in the gusset, uncertainties on ζ parameter (values between 0.01 and 0.3) control around two thirds of total leak variations, the last third being due to the variability of K_{int}^g (values between 0.64 and $3.58 \cdot 10^{-17}$ m^2). To improve knowledge on modeling input parameters, an experimental effort should preferentially be done on a better characterization of the flow reduction factor, or in practice on crack openings lower than 100 µm (both being linked).

3.3 Airproofing the Inner Side of Containments

Another practical application of the proposed strategy is its capacity to model inner side airproofing, as already carried out on EDF's assets with composite coatings. Two situations can be considered:

- Once inner coating works have been performed, the computation must be adapted to take into account new airproofed areas and forecast the most reliable possible leakage.
- Anticipating a forthcoming decennial test, the tool can model a large number of inner coatings scenarios in order to optimize the amount of work to be performed.

A proof of concept is proposed here, where the first three layers of finite elements above the raft are airproofed successively on the previous PT_0 reference computation (Tab. 7 and Fig. 13).

When the gusset is airproofed, all crack entries are sealed. Those cracks not being deviated through concrete's thickness or height, airproofing this small area is efficient and only the dome, hatch and cylindrical part contribute to the total leakage rate. Airproofing the next two layers has logically a lower impact, the leakage decrease being directly linked to the coated surface area.

4 Conclusions and Perspectives

In the context of nuclear inner containments long-term operation and life extension, a numerical methodology for computing and forecasting their air leakage rate has been developed to answer several operational needs. Numerical costs are optimized by only considering long-term behaviors representative of

containments operation (shrinkage, creep, prestessing losses, drying, crack closure and reopening), by chaining and weekly coupling THM phenomena and by discretizing with macro-elements. The full methodology has been successfully applied to the VeRCoRs mock-up and results validated during the first international benchmark associated to VeRCoRs [36].

Compared to available experimental results of the mock-up, some improvements of the proposed strategy can be considered. The chosen drying shrinkage model, suitable for long-term delayed strains, could be modified (with more parameters) to also represent short-term kinetics (Fig. 8b). The drying kinetics of core concrete also needs to be confirmed with future experimental data of the mock-up. The identification procedure, based on lab results, could be adapted to in-situ total strains measurements, for instance to define a representative creep Poisson's coefficient. As only few characterization tests are available on full-size NRB compared to VeRCoRs, this feature seems necessary. Finally, the no-early-age effect assumption of the strategy may need to be reconsidered in light of experimental observations. Concrete hydration could be added in the model as suggested by [27] to open early age cracks that would be closed by prestressing and later reopened during ILRT.

The tool implemented is suitable for supporting operators in their long-term asset management. It can be used to assess important parameters that cannot be easily measured, such as air intrinsic permeability of concrete or small openings of cracks visually inspected, and to quantify the impact of their uncertainty or variability on the total leakage rate of the containment. With better knowledge of

those inputs, air leakage forecasts become reliable to pre-empt or optimize maintenance actions (such as inner coating) to mitigate risks impacting safety and to avoid unit outage extensions and associated loss of income.

Acknowledgements

Carried out within the RSNR MACENA project, this study received government assistance handled by the French National Research Agency (ANR) under the "Investments for the future" program, part number ANR-11-RSNR-0012-01.

The authors gratefully acknowledge the VeRCoRs project team for analyzing and sharing large amounts of data as well as ERMES and MMC teams of EDF R&D for numerous discussions and for helping with *Code_Aster* and *MFront* modeling.

References

[1] https://fr.xing-events.com/EDF-vercors-project.html, VeRCoRs project website

[2] B. Masson, Démarche industrielle de comprehension des phénomènes de transferts dans les parois en béton, in: 31èmes Rencontres de l'AUGC, ENS Cachan, France, May 2013

[3] T. Wang, T. C. Hutchinson, Gas leakage through reinforced concrete shear walls: numerical study, *Nuclear Engineering and Design* 235 (2005) 2246-2260

[4] C. Nicklash, L. Coudert, G. Heinfling, C. Hervouet, B. Masson, N. Hermann, L. Stempniewski, Numerical investigation of the leakage behavior of reinforced concrete walls, in: NURETH11 International Topical Meeting on Nuclear Reactor Thermal-Hydraulics, Avignon, France, 2005

[5] M. David, Approche multi-échelle du comportement mécanique des structures en béton armé – Application aux enceintes de confinement des centrales nucléaires, Thèse, Ecole Polytechnique, 2012

[6] L. Jason, B. Masson, Comparison between continuous and localized methods to evaluate the flow rate through containment concrete structures, *Nuclear Engineering and Design* 277 (2014) 146-153

[7] X. Jourdain, Etude numérique méso-macro des propriétés de transfert des bétons fissures, Thèse, Ecole Normale Supérieure de Cachan, 2014

[8] S. Basha, R. Singh, S. Ramanujam, A. Ghosh, H. Kushwaha, Post Test Evaluation of Pre-Stressed Concrete Containment Vessel Model with BARC Finite Element Code ULCA, in: SMiRT 19 International Conference on Structural Mechanics in Reactor Technology, Toronto, Canada, 2007

[9] H. Grebner H., J. Sievert, Structural mechanics simulation of SANDIA large scale experiments on a pre-stressed concrete containment model, in: EUROSAFE Forum "Nuclear safety: new challenges, gained experience and public expectations", Paris, France, 2011

[10] H. P. Lee, Shell finite element of reinforced concrete for internal pressure analysis of nuclear containment building, *Nuclear Engineering and Design* 241 (2011) 515-525

[11] D. J. Naus, C. B. Oland, B. R. Ellingwood, H. L. Graves, W. E. Norris, Aging management of containment structures in nuclear power plants, *Nuclear Engineering and Design* 166 (1996) 367-379

[12] D. Gandhi, S. K. Chakrabarti, P. C. Basu, A study on the local behaviour of steel-concrete interfaces at and around large openings in the PSC inner containment dome, *Nuclear Engineering and Design* 239 (2009) 442-454

[13] P. Lundqvist, L.-O. Nilsson, Evaluation of prestress losses in nuclear reactor containments, *Nuclear Engineering and Design* 241 (2011) 168-176

[14] M. Mozayan, L. Davenne, S. Ghavamian, Modelling of leaktightness degradation of reinforced containment vessels due to aging and cracking mechanisms, in: SSCS 2012 Numerical Modeling Strategies for Sustainable Concrete Structures, Aix-en-Provence, France, 2012

[15] AFNOR, NF EN 1992-1-1: Eurocode 2 Calcul de structures en béton, Partie 1-1 Règles générales et règles pour les bâtiments, 2005

[16] M. Asali, Modélisation et prévision du comportement thermo-hydro-mécanique d'une paroi en béton: application au cas des enceintes de confinement des bâtiments réacteurs nucléaires, Thèse, Université Lille 1, 2016

[17] M. Asali, B. Capra, J. Mazars, J.-B. Colliat, Numerical Strategy for Forecasting the Leakage Rate of Inner Containments in Double-Wall Nuclear Reactor Buildings, *Journal of Advanced Concrete Technology* 14 (2016) 408-420

[18] L. Granger, Comportement différé du béton dans les enceintes de centrales nucléaires : analyses et modélisation, Thèse, Ecole Nationale des Ponts et Chaussées, 1995

[19] J. Verdier, Contribution à la caractérisation de l'évolution du taux de fuite des enceintes de confinement du parc nucléaire, Thèse, Université Paul Sabatier Toulouse, 2001

[20] L. Jason, Relation endommagement perméabilité pour les bétons: application aux calculs de structures, Thèse, Ecole Centrale de Nantes, 2004

[21] C. De Sa, Etude hydro-mécanique et thermo-mécanique du béton - Influence des gradients et des incompatibilités de deformation, Thèse, Ecole Normale Supérieure de Cachan, 2007

[22] E. Drouet, Impact de la température sur la carbonatation des matériaux cimentaires – Prise en compte des transferts hydriques, Thèse, Ecole Normale Supérieure de Cachan, 2010

[23] M. T. Van Genuchten, A closed-form equation for predicting the hydraulic conductivity of unsaturated soils, *Soil Science Society of America Journal* 44 (1980) 892-898

[24] Y. Mualem, New model for predicting hydraulic conductivity of unsaturated porous media, *Water Resources Research* 12 (1978) 513-522

[25] AFCEN, EPR Technical Code for Civil works, Association Française pour les règles de Conception, de construction et de surveillance en exploitation des matériels des Chaudières Electro Nucléaires, Lyon, 2010

[26] Z. P. Bazant, F. H. Wittman, Creep and shrinkage of concrete structures, chapter “Creep and shrinkage mechanisms”, Wiley, Chichester, 1982

[27] A. Hilaire, Etude des déformations différées des bétons en compression et en traction, du jeune âge au long terme, Thèse, Ecole Normale Supérieure de Cachan, 2014

[28] Z. P. Bazant, J. C. Chern. Concrete creep at variable humidity: constitutive law and mechanism, *Materials and Structures* 18 (1985) 1-20

[29] G. Pickett, The effect of change in moisture content on the creep of concrete under a sustained load, *ACI Journal Proceedings* 38 (1942) 333-355

[30] J. Mazars, F. Hamon, S. Grange, A new 3D damage model for concrete under monotonic, cyclic and dynamic loadings, *Materials and Structures* 48 (2015) 3779-3793

[31] A. Hillerborg, M. Modeer, P. E. Petersonn, Analysis of crack formation and growth in concrete by mean of fracture mechanics and finite elements, *Cement and Concrete Research*, 6 (1976) 773-782

[32] M. Matallah, C. La Borderie, O. Maurel, A practical method to estimate crack openings in concrete structures, *International Journal for Numerical and Anaytical Methods in Geomechanics*, 34 (2010) 1615-1633

[33] http://web-code-aster.org/spip.php?rubrique2, Code_Aster website, Structures and Thermomechanics Analysis for Studies and Research

[34] http://tfel.sourceforge.net/, MFront website, A code generation tool dedicated to material knowledge

[35] S. Michel-Ponnelle, Modélisation des câbles de précontrainte, Documentation de référence Code_Aster R7.01.02, 2013

[36] M. Corbin, M. Garcia, International Benchmark VeRCoRs 2015: Overview, synthesis and lessons learnt, EDF SEPTEN, 2016

[37] L. J. Klinkenberg, The permeability of porous media to liquids and gases, *API Drilling and Production Practice*, (1941) 200-213

[38] P. Mivelaz, Etanchéité des structures en béton armé: Fuites au travers d'un élément fissure, Thèse, Ecole Polytechnique Fédérale de Lausanne, 1996

[39] B. Gérard, Contribution des couplages mécanique-chimie: transfert dans la tenue à long terme des ouvrages de stockage de déchets radioactifs, Thèse, Ecole Normale Supérieure de Cachan, 1996

[40] M. Ismaïl, Etude des transferts et de leurs interactions avec la cicatrisation dans les fissures pour prolonger la durée de service des infrastructures, Thèse, Institut National des Sciences Appliquées de Toulouse, 2006

Tables

Tab. 1: Modeling and material parameters

Symbol	Value	Unit	Source
ρ_b	2395	$kg \cdot m^{-3}$	Mean value of lifts
C_p	880	$J \cdot kg^{-1} \cdot K^{-1}$	Lab test result
$\lambda(T)$	6.77T – 239	$W \cdot m^{-1} \cdot K^{-1}$	Lab test result
η_l	$1.002 \cdot 10^{-3}$	Pa·s	Reference value
ϕ	0.146	-	Mean value of lifts
E_a	28000	$J \cdot mol^{-1}$	Lab test result

R	8.314	$J \cdot mol^{-1} \cdot K^{-1}$	Reference value
T^{ref}	20 (293.15)	°C (K)	Lab test condition
K_{int}^{l}	$6.0737 \cdot 10^{-20}$	m^2	Identification on weight loss curve
n	1.3014	-	Identification on weight loss curve
P_r	$17.607 \cdot 10^{6}$	Pa	Identification on weight loss curve
E	36.849	Pa	Mean value of lifts
ν	0.2	-	Default value (no info)
α_{th}	$1.22 \cdot 10^{-5}$	K^{-1}	Mean value of lifts
ν_{bc}	0.2	-	Default value (no info)
A_t	0.9	-	Default value (no info)
B_t	variable	-	Function of fracture energy (100 $N \cdot m^{-1}$), mean tensile strength (3.89 MPa) and finite element size
A_c	1,25	-	Default value (no info)
B_c	600	-	Default value (no info)
κ_{ds}	$1.0265 \cdot 10^{-3}$	-	Identification on 1D shrinkage test
k_{rev}	168.22	Pa	Identification on 1D basic creep test
η_{rev}	$141.84 \cdot 10^{6}$	Pa·s	Identification on 1D basic creep test
k_{irr}	81.63	Pa	Identification on 1D basic creep test
κ_{dc}	$6.8968 \cdot 10^{-11}$	Pa^{-1}	Identification on 1D total creep test
M_g	$29 \cdot 10^{-3}$	$kg \cdot mol^{-1}$	Reference value
η_g	$1.8 \cdot 10^{-5}$	Pa·s	Reference value

Tab. 2: Evolution of measured total air leakage rate and distribution (in $Nm^3 \cdot h^{-1}$)

ILRT	Total	Gusset	Hatch	Cylinder	Dome
PT_0	7.7 (100 %)	4.31 (55.9 %)	1.18 (15.4 %)	1.91 (24.8 %)	0.3 (3.9 %)
PT_1	9.5	-	-	-	-
DT_1	-	-	-	-	-

Tab. 3: Values of K_{int}^{g} and w identified function of ζ. Total leakage and gusset contribution computed are compared with experimental measurements (percentage in italics)

	Identified parameter		Leakage rate ($Nm^3 \cdot h^{-1}$)	
ζ	K_{int}^{g} (10^{-17} m^2)	w (µm)	Total	Gusset
1.0	2.11	22.0	7.76 *(+0.8 %)*	4.30 *(-0.2 %)*
0.1	2.11	47.4	7.76 *(+0.8 %)*	4.30 *(-0.2 %)*

Tab. 4: Comparison of forecast and measured total leakage rates ($Nm^3 \cdot h^{-1}$) of VeRCoRs mock-up

ILRT	Measure	Computation	Relative difference
PT_0	7.7	7.76	+0.8 %
PT_1	9.5	9.71	+2.2 %
DT_1	-	12.8	-

Tab. 5: Impact of uncertainty of ζ on the total leakage computed during PT_0

Case	ζ		Total leakage rate ($Nm^3 \cdot h^{-1}$)	
ζ_{ref}	0.1		7.76	
ζ_{min}	0.01	(-90 %)	3.36	(-56.7 %)
ζ_{max}	0.3	(+200 %)	17.8	(+129 %)

Tab. 6: Impact of variability of K_{int}^{g} on the total leakage computed during PT_0

Case	K_{int}^{g} (10^{-17} m^2)		Total leakage rate ($Nm^3 \cdot h^{-1}$)	
K_{ref}	2.11		7.76	
K_{min}	0.64	(-69.7 %)	5.89	(-24.1 %)
K_{max}	3.58	(+69.7 %)	9.84	(+26.8 %)

Tab. 7: Evolution of computed leakage rate function of inner airproofing (decrease from total leakage in italics)

Inner coating	Total leak rate ($Nm^3 \cdot h^{-1}$)		Ratio of airproofed surface
None (reference)	7.76		0 %
First layer (gusset)	3.51	*(-54.8 %)*	3.77 %
Up to second layer	3.35	*(-56.8 %)*	8.73 %
Up to third layer	3.18	*(-59.0 %)*	13.7 %

Figures

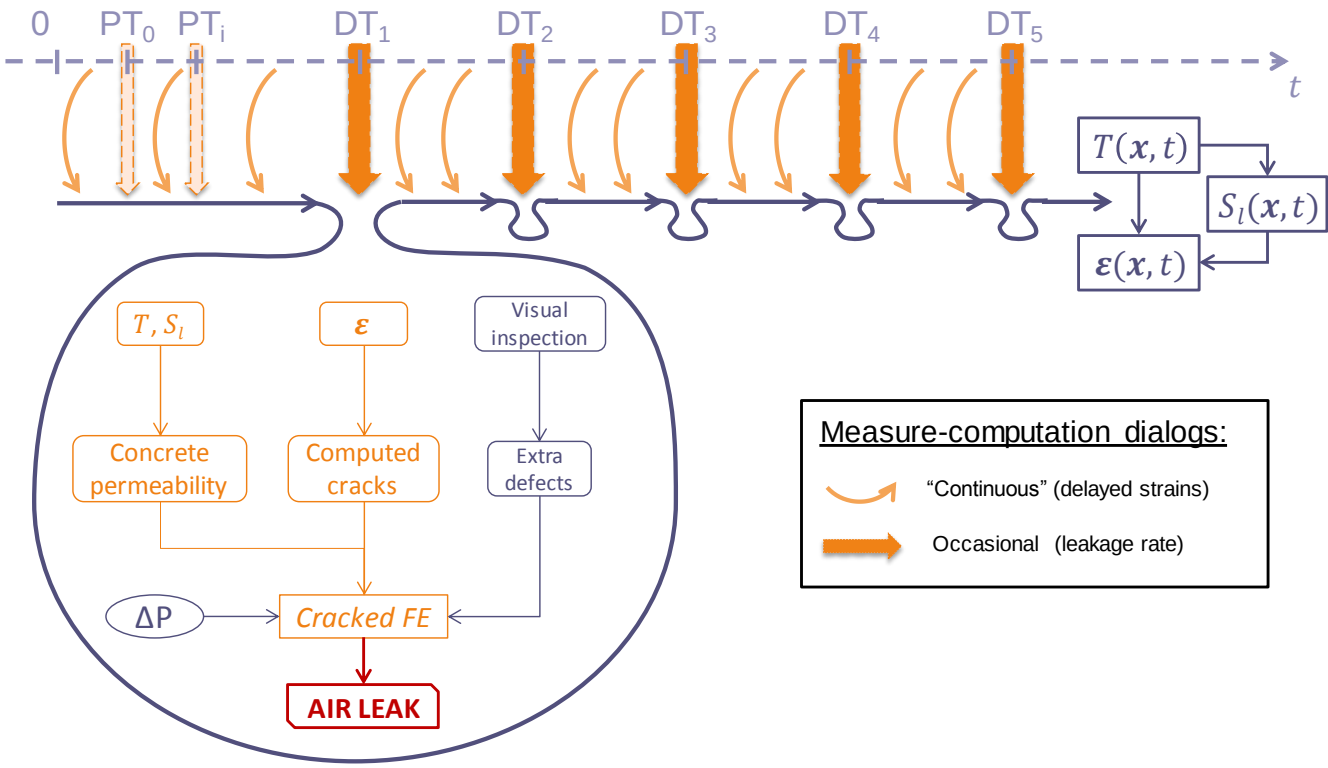

Fig. 1: Representation of the overall methodology (PT = pre-operational test, DT = decennial test). [2 columns]

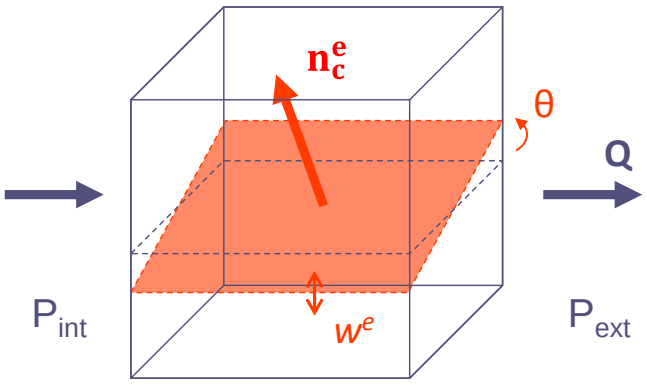

Fig. 2: Principle of the cracked finite element for air leakage computation [1 column]

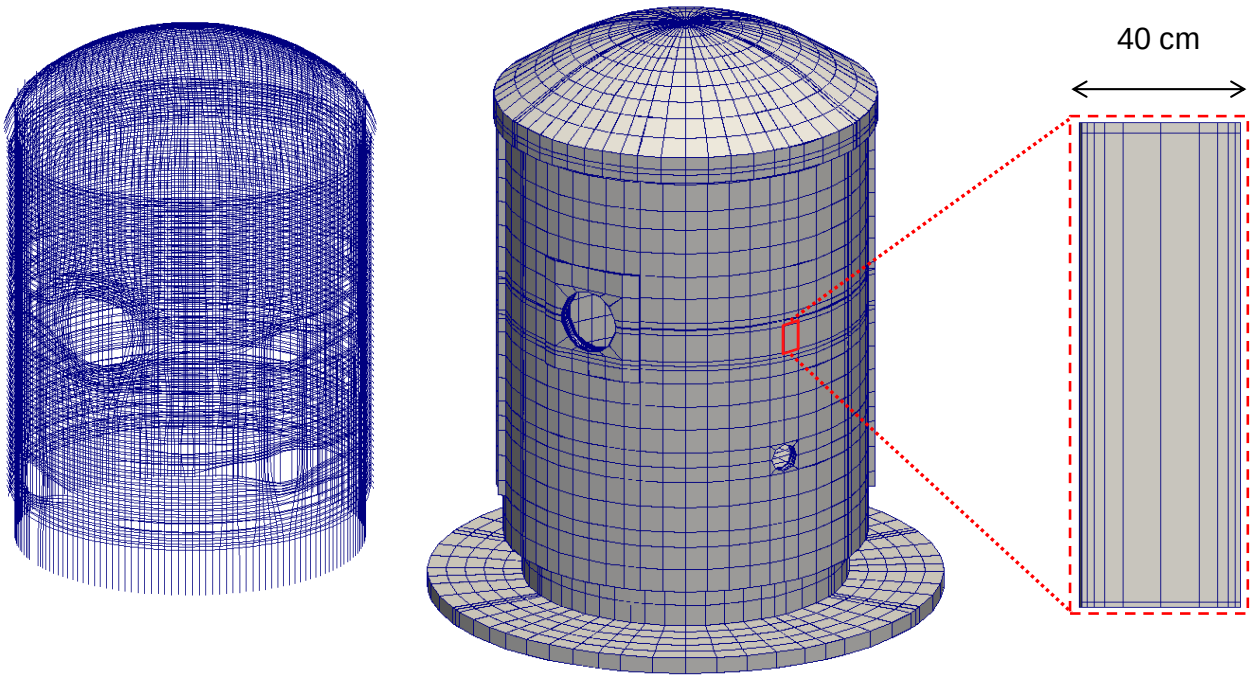

(a) Prestressing cables (b) Concrete (c) Zoom on thickness

Fig. 3: Overview of the coarse mesh of the mock-up [2 columns]

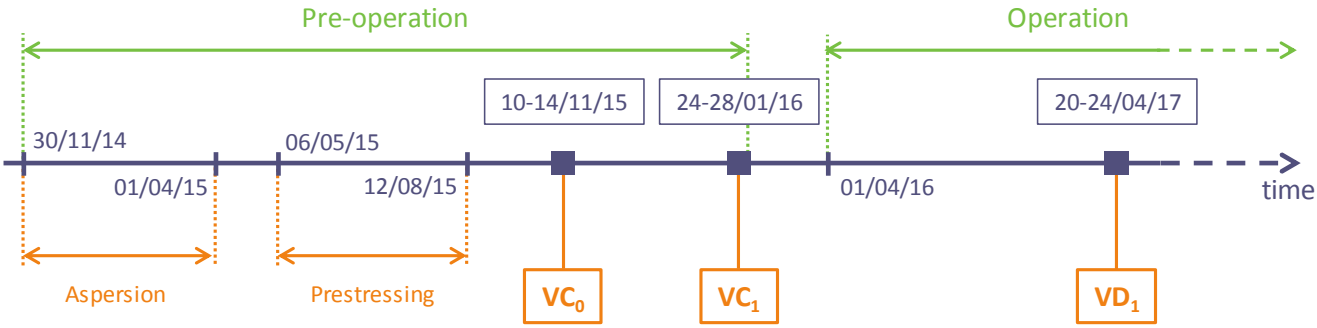

Fig. 4: Overall planning considered for computations on VeRCoRs mock-up [2 columns]

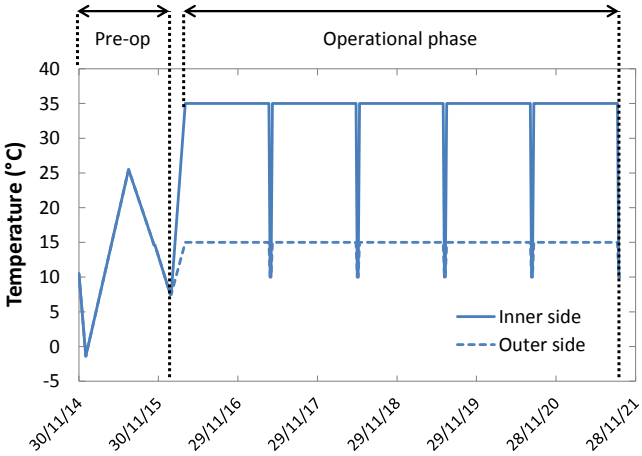

Fig. 5: Evolution of temperature imposed at both sides of the inner containment [1 column]

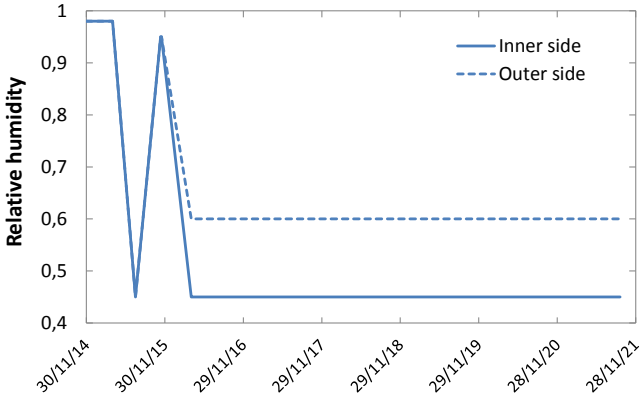

Fig. 6: Evolution of relative humidity imposed at both sides of the inner containment [1 column]

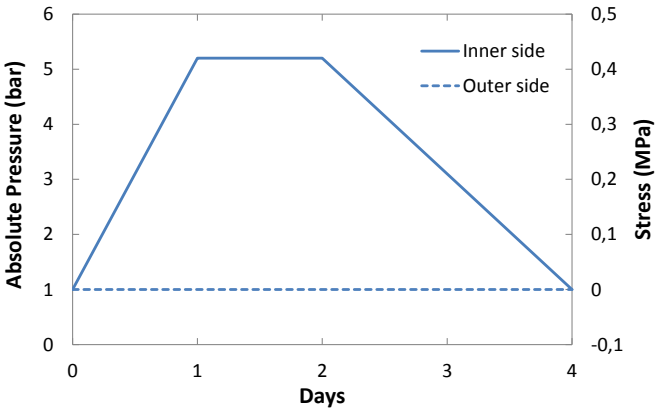

Fig. 7: Evolution of air pressure imposed at both sides of the inner containment [1 column]

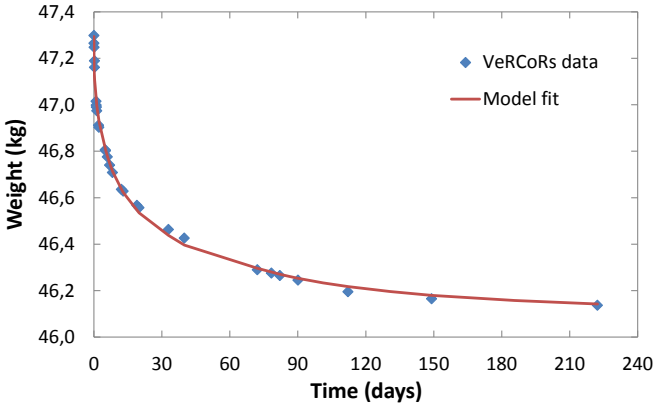

(a) Weight loss

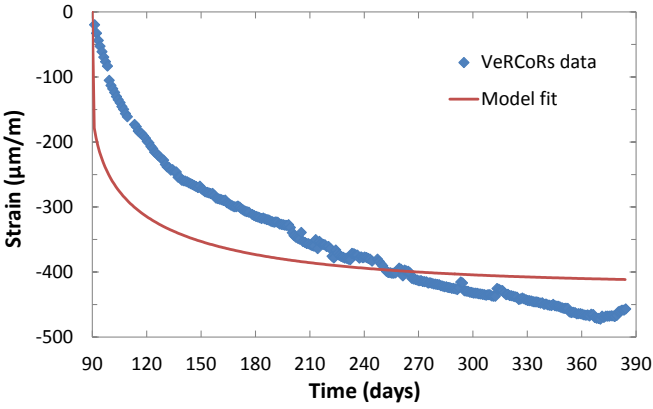

(b) 1D drying shrinkage

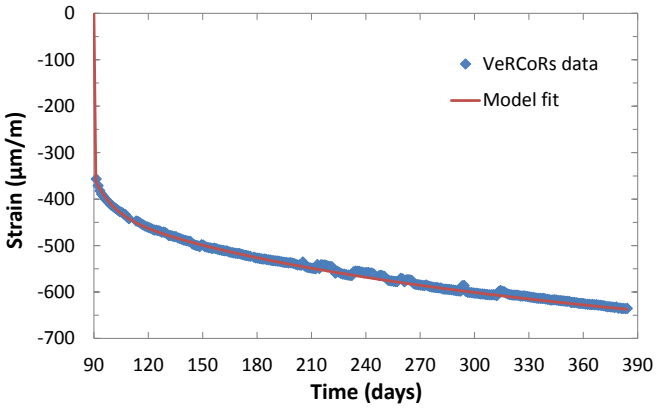

(c) 1D basic creep

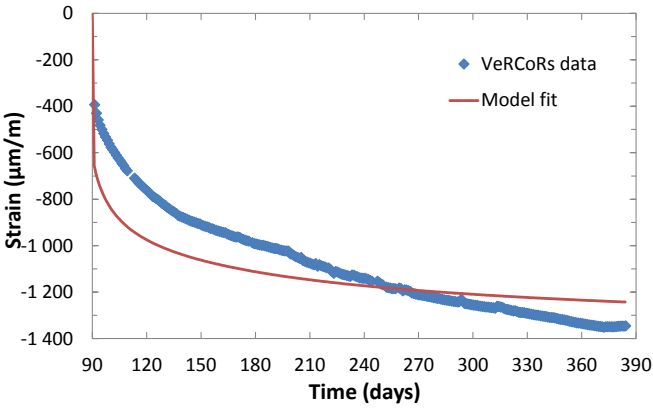

(d) 1D total creep

Fig. 8: Identification of some model parameters from lab measurements [2 columns]

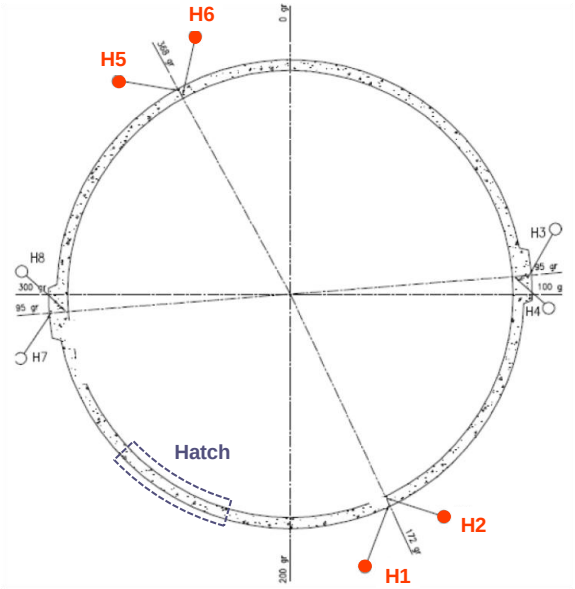

Fig. 9: Localization of observation points H1, H2, H5 and H6 [1 column]

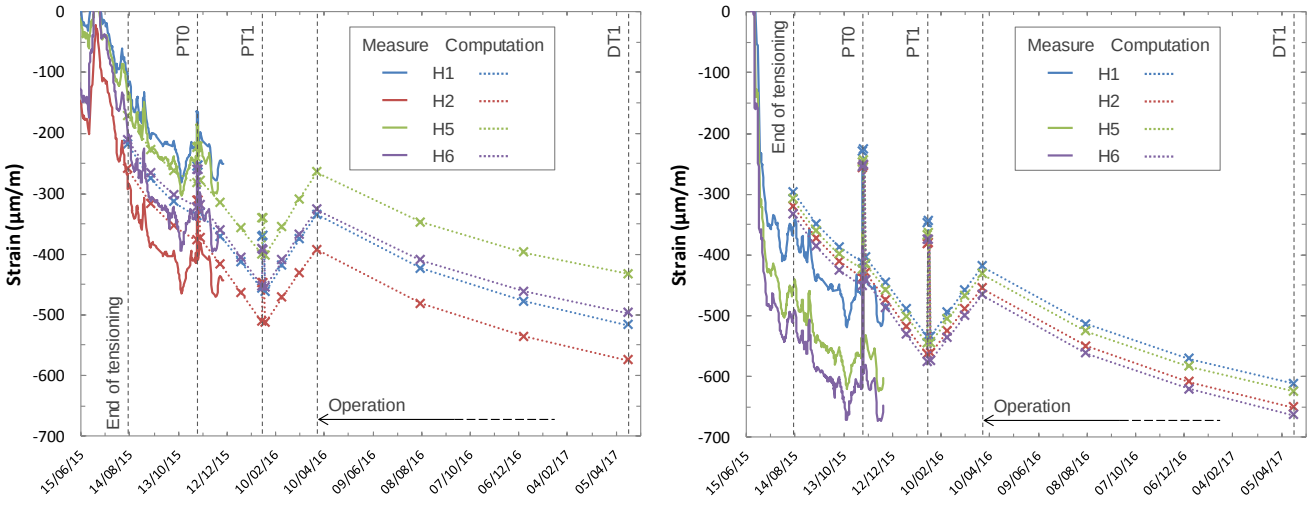

(a) Vertical strains (b) Tangential strains

Fig. 10: Evolution of measured and computed total strains at points H1, H2, H5 and H6 [2 columns]

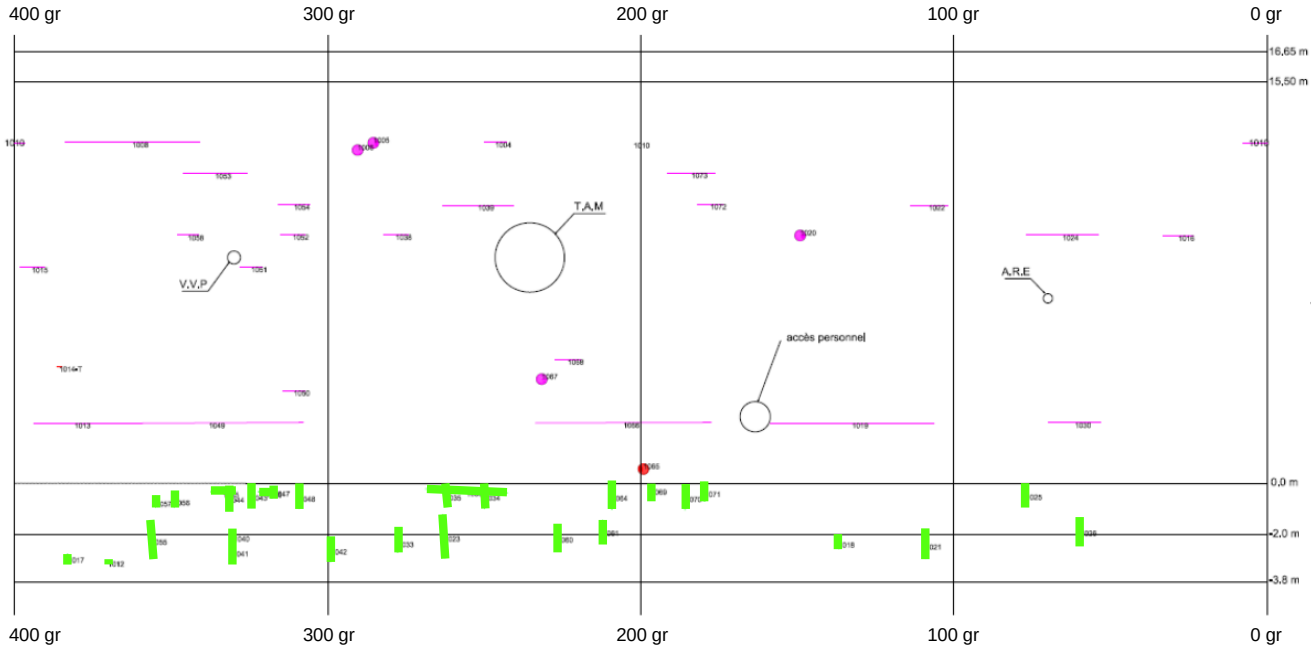

Fig. 11: Visual inspection of the outer side of the mock-up after PT_0 (cracks in bold green, [36]) [2 columns]

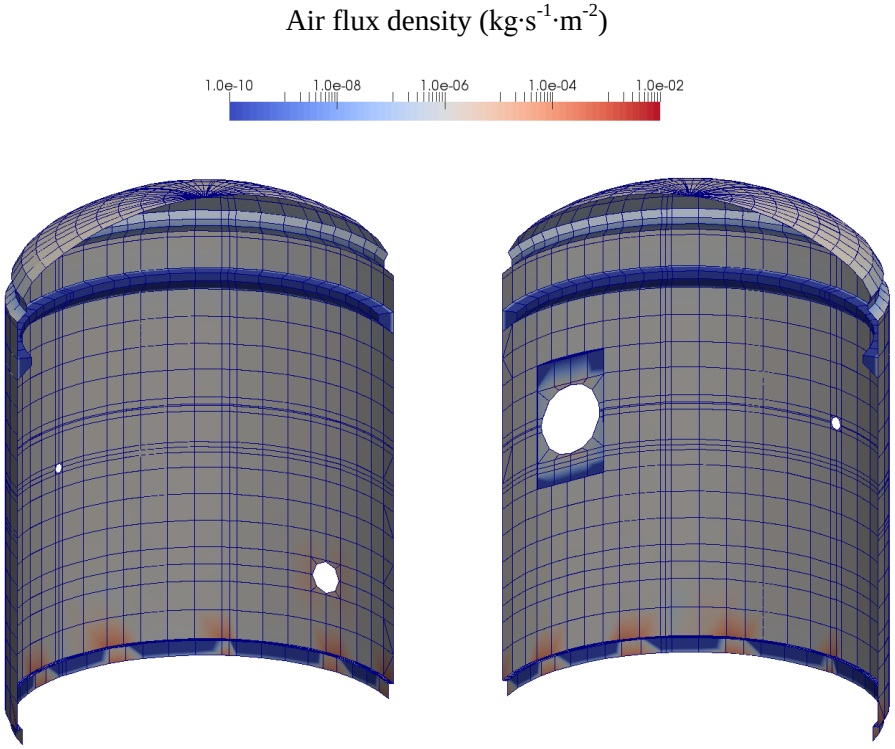

(a) 0-200 gr (b) 200-400 gr

Fig. 12: Norm of air mass nodal fluxes computed at the inner side of the mock-up during PT_0 (influence of cracks in the gusset) [1.5 column]

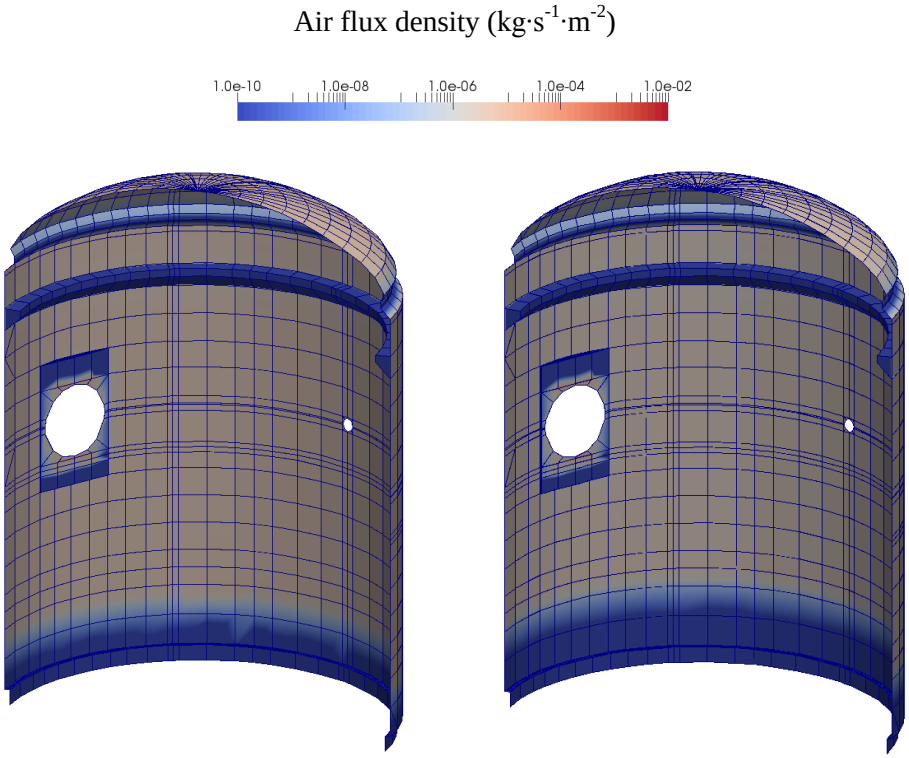

(a) Coating up to the second layer (b) Coating up to the third layer

Fig. 13: Norm of air mass nodal fluxes computed at the inner side of the mock-up during PT_0 (influence of airproofing, 200-400 gr) [1.5 column]